# Focusing XFEL SASE pulses by rotationally parabolic refractive x-ray lenses



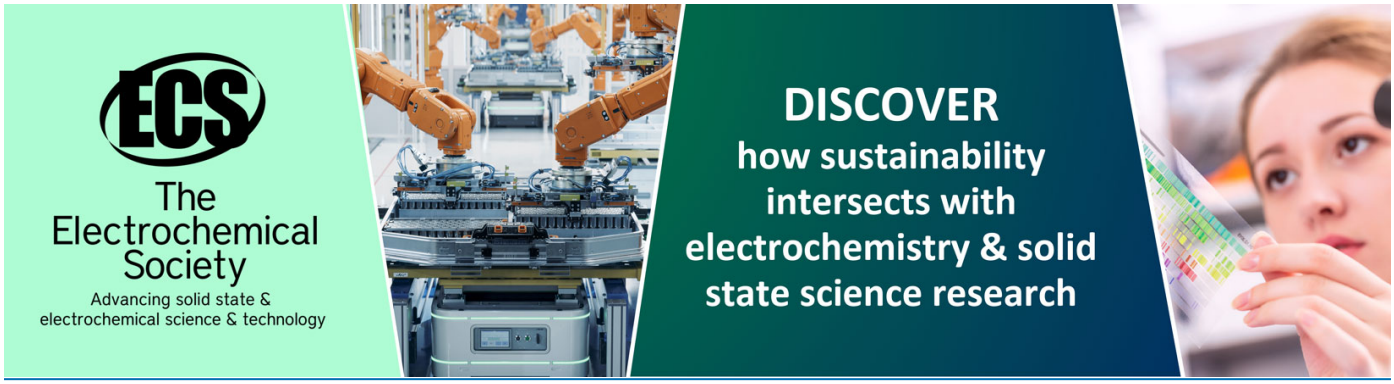

Journal of Physics: Conference Series **499** (2014) 012004 doi:10.1088/1742-6596/499/1/012004

# Focusing XFEL SASE pulses by rotationally parabolic refractive x-ray lenses

**Frank Seiboth[1], Andreas Schropp[1,2], Robert Hoppe[1], Vivienne Meier[1], Jens Patommel[1], Hae Ja Lee[2], Bob Nagler[2], Eric C. Galtier[2], Brice Arnold[2], Ulf Zastrau[2], Jerome B. Hastings[2], Daniel Nilsson[3], Fredrik Uhlén[3], Ulrich Vogt[3], Hans M. Hertz[3], Christian G. Schroer[1]**

[1]Institute of Structural Physics, Technische Universität Dresden, D-01062 Dresden, Germany
[2]Linac Coherent Light Source, SLAC National Accelerator Laboratory, 2575 Sand Hill Road, Menlo Park, CA 94025, USA
[3]Biomedical & X-Ray Physics, KTH/Royal Institute of Technology, KTH-AlbaNova, SE-106 91, Stockholm, Sweden

E-mail: schroer@xray-lens.de

**Abstract.** Using rotationally parabolic refractive x-ray lenses made of beryllium, we focus hard x-ray free-electron laser pulses of the Linac Coherent Light Source (LCLS) down to a spot size in the 100 nm range. We demonstrated efficient nanofocusing and characterized the nanofocused wave field by ptychographic imaging [A. Schropp, et al., Sci. Rep. **3**, 1633 (2013)] in the case of monochromatic LCLS pulses produced by a crystal monochromator that decreases the LCLS bandwidth down to $\Delta E/E = 1.4 \cdot 10^{-4}$. The full spectrum of LCLS pulses generated by self-amplified spontaneous emission (SASE), however, fluctuates and has a typical bandwidth of a few per mille ($\Delta E/E \approx 2 \cdot 10^{-3}$). Due to the dispersion in the lens material, a polychromatic nanobeam generated by refractive x-ray lenses is affected by chromatic aberration. After reviewing the chromaticity of refractive x-ray lenses, we discuss the influence of increased bandwidth on the quality of a nanofocused SASE pulse.

## 1. Introduction

The ultra-short pulses of x-ray free-electron lasers open the way for the investigation of the dynamics of matter on atomic time and length scales. Focusing these pulses to 100 nanometers and below is crucial for many experiments, such as high-resolution and time-resolved imaging with single pulses, the study of non-linear optical phenomena, and the creation of matter in extreme conditions [1, 2, 3, 4, 5]. Several optics have been shown to be capable of focusing XFEL pulses to these small dimensions, such as Fresnel zone plates [6, 7], Kirkpatrick-Baez mirrors [8], and refractive x-ray lenses [9].

Today, refractive x-ray optics are widely spread at synchrotron radiation sources and are typically used in conjunction with a crystal monochromator. For monochromatic radiation, e. g., a relative bandwidth of $\Delta E/E = 1.4 \cdot 10^{-4}$ for Si (111) reflections, chromatic aberrations of refractive x-ray lenses are negligible. The typical bandwidth of an XFEL pulse generated by self-amplified spontaneous emission (SASE) is about one order of magnitude wider than that of a Si (111) crystal monochromator. In the case of the Linac Coherent Light Source (LCLS)

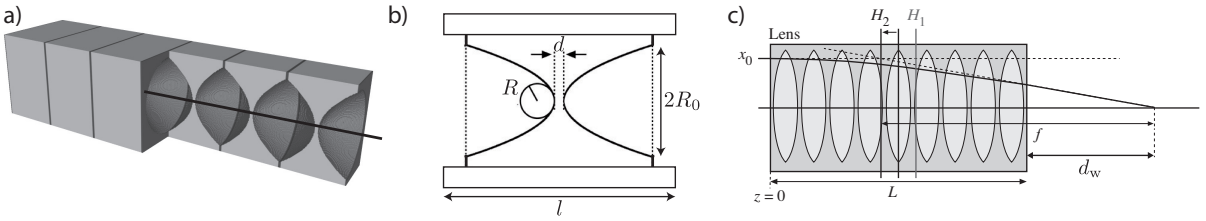


**Figure 1.** a) Rotationally parabolic refractive x-ray lens. The optic is made of a series of individual refractive x-ray lenses that are stacked behind each other. b) Parameters for individual refractive x-ray lenses. c) Thick refractive x-ray lens.

at the Stanford Linear Accelerator Center in Menlo Park, California, USA, the typical SASE bandwidth is about $\Delta E/E = 2 \cdot 10^{-3}$.

In this article we investigate the effect of this mild polychromaticity on the nanofocusing capabilities of parabolic refractive x-ray lenses using geometric arguments. Alternatively, an approach using longitudinal coherence could be followed, as demonstrated for diffractive optics [10]. For an ideal parabolic refractive lens and a more realistic optic that shows weak spherical aberrations, we model the intensity distribution around the nominal focus for monochromatic radiation, Gaussian spectral distributions of different width, and for a more realistic SASE spectrum. In a recent experiment, we focused monochromatic XFEL radiation to the 100 nanometer level by parabolic refractive x-ray lenses made of beryllium and characterized the nanobeam using the method of ptychography [9, 11]. Using the complex wave field reconstructed in this way, we calculate the chromatic aberrations of the optics and its consequences for nanofocusing.

## 2. Characterizing XFEL pulses by ptychography

We used ptychography to characterize the nanofocused x-ray pulses of the LCLS. A detailed account of this experiment can be found in [9]. The x-ray pulses were focused by parabolic refractive x-ray lenses made of beryllium [12, 13]. The compound lens was made of $N = 20$ single lenses with a radius of curvature $R = 50\,\mu$m. The aperture was defined by a pinhole to $300\,\mu$m [cf. Fig. 1]. The expected diffraction limited focal spot size for this optic is 115 nm (full width half maximum, FWHM).

The experiments were carried out at the Matter in Extreme Conditions (MEC) endstation located 464 m downstream of the SASE undulator in the far experimental hall of LCLS. A Bartel type monochromator was used to filter the beam to a relative bandwidth of $\Delta E/E \approx 1.4 \times 10^{-4}$ at an energy of $E = 8.194\,$keV.

In order to characterize the nanofocused XFEL pulses, we recorded a ptychogram of a test sample. Ptychography is a scanning coherent diffraction imaging technique, in which a sample is scanned through a confined coherent x-ray beam in two dimensions perpendicular to the optical axis [14, 15]. At each position of the scan, a far-field diffraction pattern is recorded. The step size in between adjacent scan points is chosen such that the illuminated areas overlap. From these data, the complex transmission function of the object and the complex illuminating wave field in the plane of the sample can be reconstructed [16, 17, 18]. This method is ideal for quantitative x-ray imaging with highest spatial resolutions [19, 20, 21, 22] even in three dimensions [23, 24, 25]. Using a test object, the coherent beam can be fully characterized by ptychography [26, 27, 28, 29], giving access to the full caustic [30]. By now, the method is routinely applied to characterize x-ray nanofocusing optics at synchrotron radiation sources and the beam properties of hard x-ray scanning microscopes [31].

The test sample was placed into the XFEL beam about 0.5 mm downstream of the focal

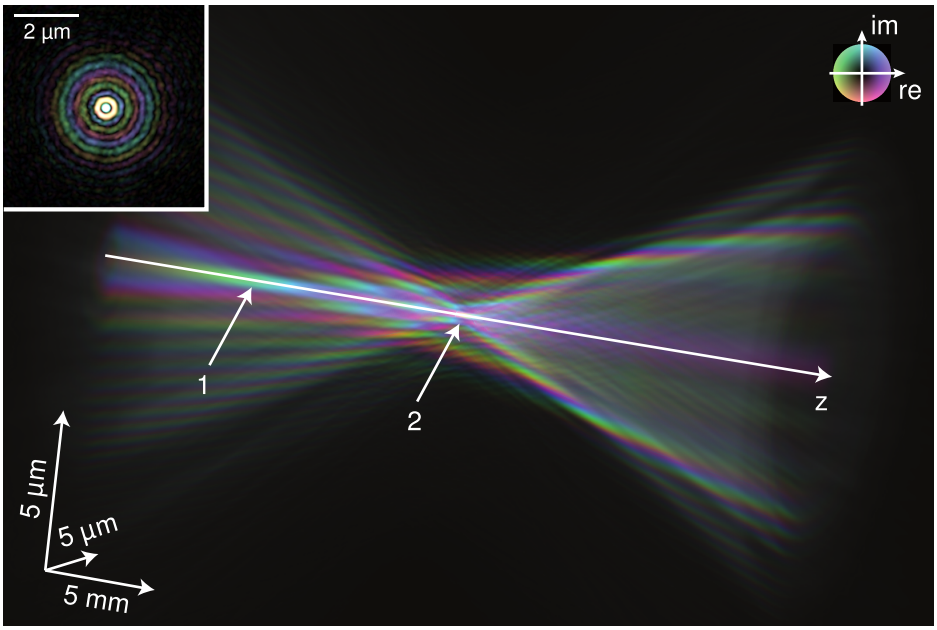


**Figure 2.** Reconstructed complex wave field propagated ±15 mm along the optical axis. Phase is encoded in color, amplitudes in hue. The caustic reveals a spherical aberration of the refractive x-ray optics, as the paraxial rays are focused to a shorter focal length (pointed to by arrow 1) whereas the peripheral rays coincide at a larger focal distance (pointed to by arrow 2). The inset shows the up-scaled wave field near position two.

plane and scanned on a two-dimensional grid perpendicular to the beam, covering an area of $2 \times 2\,\mu\text{m}^2$ with a step size of 100 nm. The test sample was nanostructured into a 1 $\mu$m-thick tungsten layer sputter deposited onto a 100 $\mu$m-thick CVD diamond substrate. The test patterns were arranged in an array of $40 \times 40$ identical star patterns, each approximately $2 \times 2\,\mu\text{m}^2$ in size with structures ranging from 50 nm to 200 nm. As monochromatized XFEL pulses strongly fluctuate in intensity, two diffraction patterns were recorded at each scan point with a Princeton Instruments PIXIS-XF 2048B x-ray camera located 4.14 m behind the focus.

For the ptychographic reconstruction, only diffraction patterns with intensities above a certain threshold were selected and normalized to the pulse intensity [9]. The ptychographic reconstruction yields both the complex transmission function of the object and a complex wave field. Since the ptychographic dataset is created by a large number of individual XFEL pulses, each slightly varying in shape and intensity, the complex illumination function represents an averaged illumination function produced by the nanofocusing optics. It yields detailed information about the nanofocused x-ray beam and is shown in the inset in Fig. 2. As the wave field is given in amplitude and phase, it can be used to reconstruct the full caustic near the nanofocus (Fig. 2) or to model near field images recorded in magnifying geometry [32].

In the following, we use this wave field to model the intensity distribution around the focus in the case of mild polychromaticity, i. e., for x-ray spectra with a bandwidth typical to SASE XFELs.

## 3. Chromaticity of x-ray lenses and limitations to focusing SASE pulses

The focal length of a compound refractive lens (CRL) is

$$f = \frac{1}{\omega \sin(\omega L)}, \quad \omega^2 = \frac{2\delta}{lR} = \beta \frac{2\delta}{R_0^2}, \tag{1}$$

where $\omega^2$ is the refractive power per unit length. $R$ is the radius of curvature of the parabolic surfaces of a single biconcave lens, $l$ its overall length, and $\delta$ the index of refraction decrement of the lens material [cf. Fig. 1b) and eq. (2) below]. $\omega^2$ can be expressed in terms of the geometric aperture radius $R_0$ by introducing a geometric factor $\beta := R_0^2/(lR) < 1$ [Fig. 1b)]. $L = Nl$ is the overall length of the compound lens made of $N$ individual lenses [Fig. 1c)]. In this article, CRLs are treated as thick optics, unless $L$ is small compared to the focal length $f$, in which case the lens can be treated as optically thin.

For a complex refractive index $n = 1 - \delta + i\beta$, $\delta$ is given by

$$\delta = \frac{n_\mathrm{a}}{2\pi} r_0 \lambda^2 \left[ f_0(K=0) + f'(E) \right] \tag{2}$$

in the hard x-ray range. Here, $n_\mathrm{a}$ is the number density of the atoms in the lens material, $r_0$ the classical electron radius, $\lambda$ the wavelength of the x rays, and $f_0 + f'$ the real part of the atomic form factor in forward direction. Away from absorption edges of the lens material, $f'$ is nearly negligible and $f_0 = Z$ corresponds to the atomic number of the material. Therefore, $\delta$ scales inversely with the square of the energy ($\delta \propto E^{-2}$) for beryllium lenses in the hard x-ray range.

From eqs. (1) and (2) the relative change in focal distance $f$ as a function of energy can be derived:

$$\frac{\Delta f}{f} = \underbrace{\left[1 + \omega L \cot(\omega L)\right]}_{=:\gamma} \frac{\Delta E}{E}. \tag{3}$$

For thin lenses, $\omega L$ is much smaller than one and $\Delta f/f = 2\Delta E/E$. For the thickest conceivable lens, i. e., when the focus is at the exit of the lens stack, $\gamma = 1$.

This chromaticity can be tolerated for nanofocusing, if the lateral beam size as a result of the chromaticity is smaller than the diffraction limited beam size, i. e.,

$$\Delta f \cdot NA \leq d_t = \alpha \frac{\lambda}{2NA}, \tag{4}$$

which is equivalent to require $\Delta f$ to be smaller or equal to the depth of focus. In general, $\alpha$ depends on the aperture function of the optic and the resolution criterium. For refractive lenses with Gaussian aperture, $d_t$ is the full width at half maximum of the Gaussian Airy disc and $\alpha = 2\sqrt{2\ln 2}/\pi \approx 0.75$ [12]. $NA$ is the numerical aperture given by

$$NA = \frac{D_\mathrm{eff}}{2f}, \quad D_\mathrm{eff} = 2\frac{\sqrt{2\delta}}{\omega} \left\{ \frac{\beta}{a_p} \left[1 - \exp(-a_p)\right] \right\}^{1/2}, \quad a_p := \beta \frac{\mu L}{2} \cdot \underbrace{\frac{1}{2}\left[1 + \frac{\sin(2\omega L)}{2\omega L}\right]}_{=:\epsilon}. \tag{5}$$

Here, $\mu$ is the linear attenuation coefficient of the lens material. $D_\mathrm{eff}$ is the so-called effective aperture. Using eq. (4), the maximal energy bandwidth that can be tolerated in a given imaging geometry is

$$\frac{\Delta E}{E} \leq \frac{2}{\alpha\gamma} \cdot \frac{d_t^2}{\lambda f} = \alpha \frac{2}{\gamma} \cdot \frac{\lambda f}{D_\mathrm{eff}^2}. \tag{6}$$

The intensity in the nominal focal plane ($z = z_0$) is an incoherent sum over the intensities of the wave fields for the different spectral modes:

$$I_{z_0}(x,y) = \int \rho(E) |\psi(x,y,z_0,E)|^2 \, dE. \tag{7}$$

Here, $\rho(E)$ is the spectral density of the polychromatic beam and $\psi(x,y,z,E)$ is the spatial component of the wave field for a given energy $E$. The beam broadening in the nominal

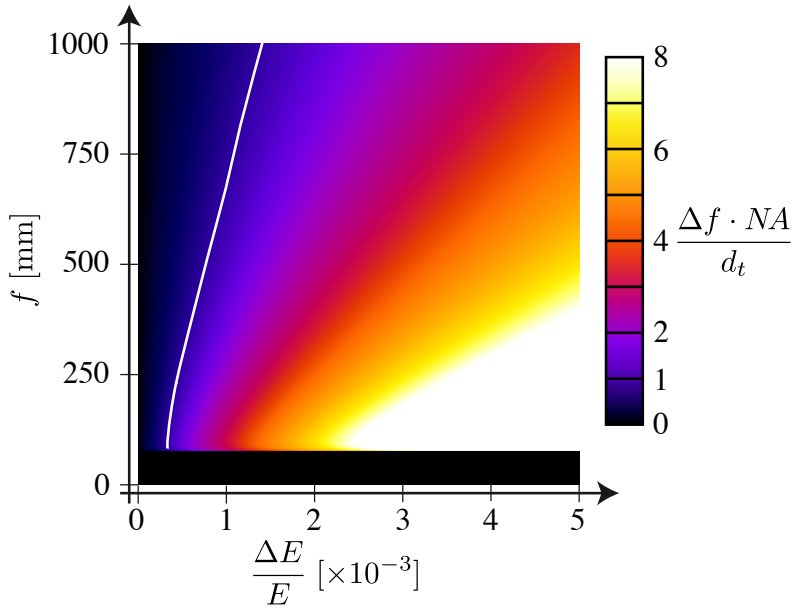


**Figure 3.** Broadening due to chromatic aberration [left-hand side of eq. (4)] relative to the diffraction limit $d_t$ [right-hand side of eq. (4)] as a function of energy bandwidth and focal length. The white line delineates the border between diffraction limited (left) and chromaticity limited focusing (right). The black area in the lower part of the graph is masking a regime where the focus would lie within the lens.

focal plane can be estimated by considering the width $b$ (FWHM) of the components of the polychromatic beam that are defocused by $\Delta f$:

$$b = \sqrt{d_t^2 + (\Delta f \cdot NA)^2} = \sqrt{d_t^2 + \left(\frac{D_{\text{eff}}}{2} \cdot \gamma \cdot \frac{\Delta E}{E}\right)^2}. \tag{8}$$

In the case of a nearly Gaussian aperture, i. e., $\exp(-a_p) \approx 0$, $D_{\text{eff}}$ and $d_t$ scale proportional to $\sqrt{f}$. In that regime, the relative influence of the chromaticity is independent of the focal length.

The refractive optics that were used in the nanofocusing experiments at LCLS are not in this Gaussian regime. The parameters are such that the Gaussian aperture is clipped by the geometric aperture. Therefore, the influence of the focal length on the chromaticity is not negligible in this case. Fig. 3 shows the fraction of the broadening due to chromatic aberration relative to the diffraction limit:

$$\frac{\Delta f \cdot NA}{d_t}.$$

If this quotient is smaller than one, the beam is dominated by the diffraction limit. If the quotient is larger than one, the nanofocus is dominated by chromatic effects. For the imaging parameters at the LCLS, i. e., $f = 250$ mm and $\Delta E/E \approx 2 \cdot 10^{-3}$, chromatic effects are already quite important, i. e., $\Delta f \cdot NA/d_t = 4.3$. In the following section, we investigate the impact of chromaticity for this particular case.

## 4. Focusing broadband x rays and SASE pulses with CRLs made of beryllium

To show the influences of broadband x rays on chromatic optics, we modeled the focusing properties for two sets of beryllium CRLs at the mean energy of $E = 8.194\,\text{keV}$. The first one is

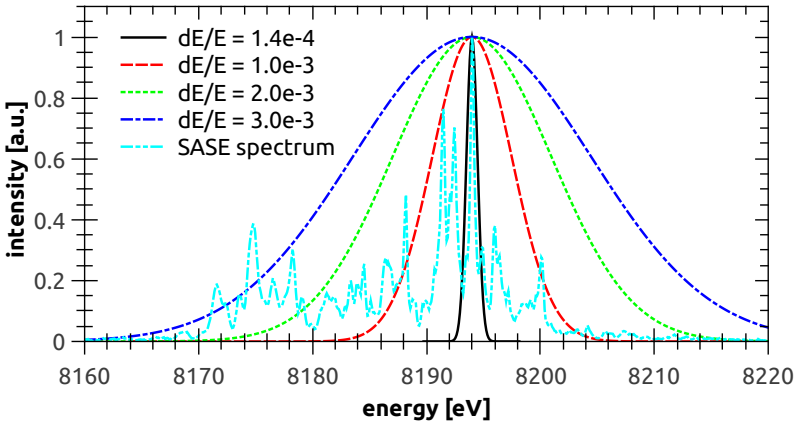


**Figure 4.** Spectral distributions used to calculate the influences of broadband XFEL beams. The Gaussian with a FWHM width of $\Delta E/E = 1.4 \cdot 10^{-4}$ models the monochromatic case. Three broader Gaussian distributions and a more realistic SASE spectrum are used to model the polychromatic beam from a SASE XFEL source.

an ideal lens (without spherical aberrations) with the same imaging parameters as the real lens that was used in the LCLS nanofocusing experiment ($N = 20, R = 50\,\mu\text{m}, 2R_0 = 300\,\mu\text{m}$). The focal spot size for this optic is expected to be 115 nm (FWHM) with a depth-of-focus of roughly 200 $\mu$m. Since the dominating effect of small energy variations is a change in focal distance [c. f. eq. (3)], the expected beam profile can be determined by overlapping a single monochromatic profile at different shifted positions along the optical axis. This assumes that the wave-front shape $\psi(x, y, z, E)$ [cf. eq. (7)] is not significantly changed for this mild polychromaticity, i. e., the focus remains similar in lateral distribution but shifts along the optical axis according to the chromatic aberration.

We calculate the intensity distribution in the nominal focal plane by the convolution of the 3-dimensional intensity distribution with the spectral distribution function mapped onto the optical axis by eq. (3). We used several spectral distribution functions and compared the focusing results. The spectral distribution functions are shown in Fig. 4.

The intensity distribution in the focal plane is shown for an ideal lens for the different energy spectra in Figure 5 a) and c). The focal spot size is already broadened at the base for $\Delta E/E = 1 \times 10^{-3}$. Reason for this is the perfect focusing characteristic of this lens that is free of spherical aberrations. The depth-of-focus is determined by the diffraction limit and is about 200 $\mu$m. Since the beam is smeared by approximately by half a millimeter along the optical axis for a polychromaticity of $\Delta E/E = 1 \times 10^{-3}$, the focal depth is clearly exceeded. Especially for the SASE spectrum one can see an even stronger broadening, since the spectral distribution is widely spread, with significant peaks well outside a Gaussian envelope (c. f. Fig. 4).

The situation is different for the optic that has a spherical aberration. To determine the intensity distribution, we made use of the measured wave field obtained during the ptychography experiment described in section 2. For this optic, the spherical aberrations lead to an elongation of the effective depth-of-focus as well as a small increase in focal spot size. Using this profile for the convolution with the exact same spectra as before, the line plots in Fig. 5 b) and d) are obtained. The focus has dominant side-lobes even for the nearly monochromatic case. When increasing the energy bandwidth, the main effect is a shift of the whole distribution to higher intensities. The shape is only changing by a margin. A more detailed look for selected spectra

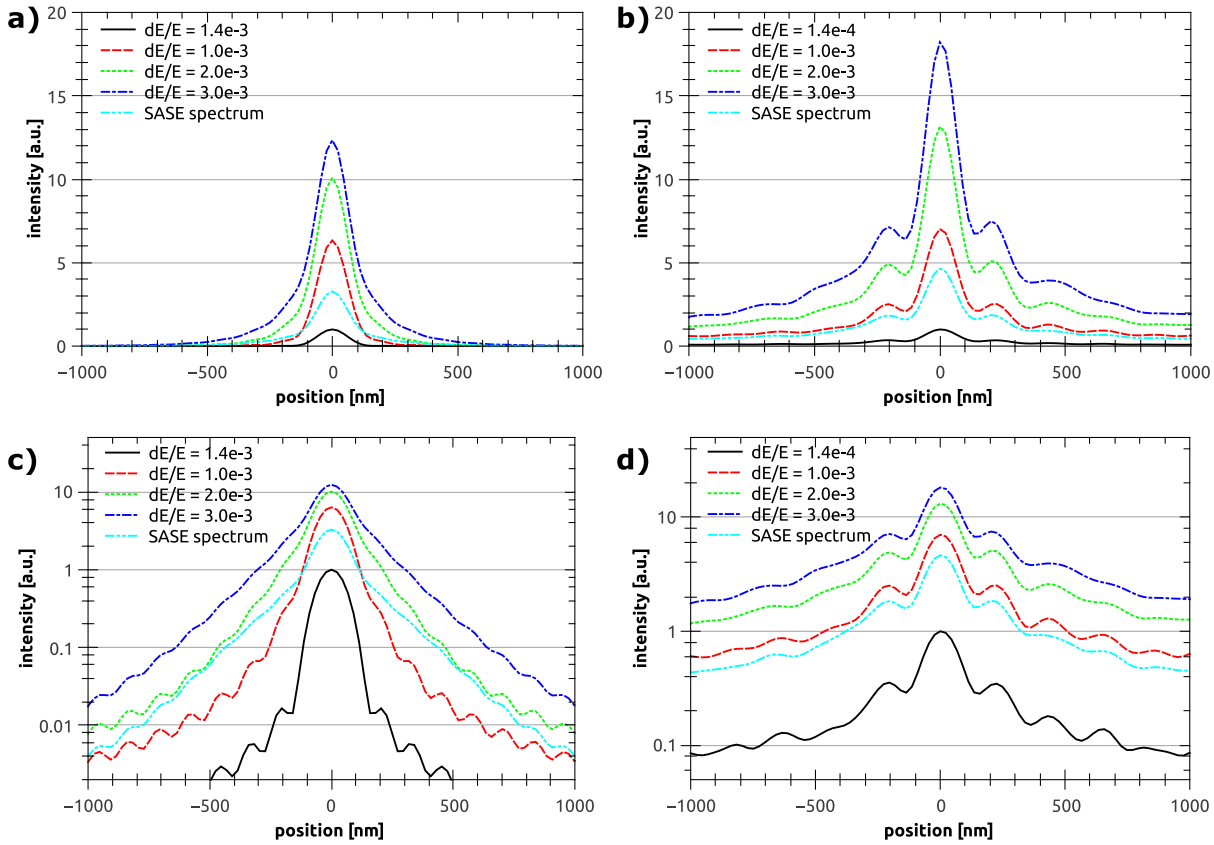


**Figure 5.** Integrated line profiles through the beam waist for an ideal parabolic optic on a linear a) and logarithmic scale c). Similar profiles for the lens with spherical aberration used during experiments at LCLS on a linear b) and logarithmic scale d).

is shown in Figure 6. The most dominant effect in the beam caustics on the left is a blurring, while the overall shape of the beam waist seems nearly unaffected. Also the sections through the beam shown in Fig. 6 on the right taken in the plane marked with a white line in the profiles (Fig. 6 left) show mostly a smearing of the side lobes, while the central peak remains almost unchanged in size.

The intensities in Fig. 5 are normalized to the peak intensity of the monochromatic beam. The relative gain in peak intensity for the polychromatic illumination is about one order of magnitude. The nanobeam generated by the ideal lens is more sensitive to chromatic aberration and thus the relative gain in peak intensity is slightly less than for the lens spherical aberration [compare Fig. 5a) and b)]. However, when comparing absolute peak intensities, the ideal optic is about a factor of five higher than the one with spherical aberration for the monochromatic case.

## 5. Conclusions

In general, the bandwidth of SASE pulses from the Linac Coherent Light Source is too large to be able to neglect chromatic effects when nanofocusing XFEL pulses with compound refractive lenses. While the full-width-half-maxium size of the beam is only slightly affected, the chromatic aberration results in a significant increase in the intensity in the shoulders and the side maxima of the beam. If the optics have spherical aberrations, the chromatic effects may be obscured by these aberrations and become dominant only for larger bandwidths. This is the case for the

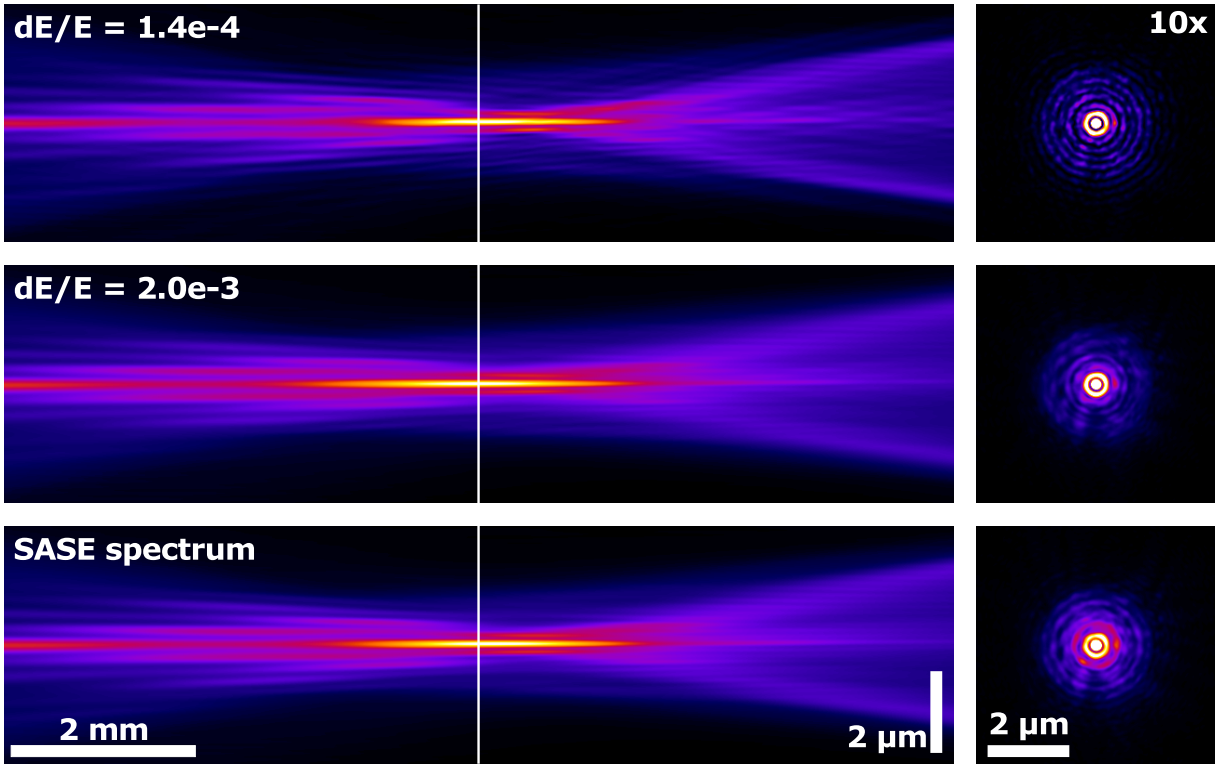


**Figure 6.** Calculated beam intensity along the caustic (left) and intensity in the focal plane marked by the white line (upscaled to show low intensity features) for the aberrated Be CRLs at different energy bandwidths (right).

parabolic refractive lenses used in our experiment at LCLS.

**Acknowledgments**
Portions of this research were carried out at the Linac Coherent Light Source (LCLS) at the SLAC National Accelerator Laboratory. LCLS is funded by the U.S. Department of Energy's Office of Basic Energy Sciences. The MEC instrument was supported by U.S. Department of Energy, Office of Fusion Energy Sciences. This work was funded by Volkswagen Foundation, the DFG under grant SCHR 1137/1-1, the German Ministry of Education and Research (BMBF) under grant number 05K13OD2, the Swedish Research Council and the Göran Gustafsson Foundation. We would also like to thank the MEC team at SLAC, collaborating institutions, and Bruno Lengeler for fruitful discussions and providing the CRL optics.

**References**

[1] Koopmann R, Cupelli K, Redecke L, Nass K, Deponte D P, White T A, Stellato F, Rehders D, Liang M, Andreasson J, Aquila A, Bajt S, Barthelmess M, Barty A, Bogan M J, Bostedt C, Boutet S, Bozek J D, Caleman C, Coppola N, Davidsson J, Doak R B, Ekeberg T, Epp S W, Erk B, Fleckenstein H, Foucar L, Graafsma H, Gumprecht L, Hajdu J, Hampton C Y, Hartmann A, Hartmann R, Hauser G, Hirsemann H, Holl P, Hunter M S, Kassemeyer S, Kirian R A, Lomb L, Maia F R N C, Kimmel N, Martin A V, Messerschmidt M, Reich C, Rolles D, Rudek B, Rudenko A, Schlichting I, Schulz J, Shoeman M M S R L, Sierra R G, Soltau H, Stern S, Strueder L, Timneanu N, Ullrich J, Wang X, Weidenspointner G, Weierstall U, Williams G J, Wunderer C B, Fromme P, Spence J C H, Stehle T, Chapman H N, Betzel C and Duszenko M 2012 *Nature Methods* **9** 259

[2] Johansson L C, Arnlund D, White T A, Katona G, Deponte D P, Weierstall U, Doak R B, Shoeman R L, Lomb L, Malmerberg E, Davidsson J, Nass K, Liang M, Andreasson J, Aquila A, Bajt S, Barthelmess M,

Barty A, Bogan M J, Bostedt C, Bozek J D, Caleman C, Coffee R, Coppola N, Ekeberg T, Epp S W, Erk B, Fleckenstein H, Foucar L, Graafsma H, Gumprecht L, Hajdu J, Hampton C Y, Hartmann R, Hartmann A, Hauser G, Hirsemann H, Holl P, Hunter M S, Kassemeyer S, Kimmel N, Kirian R A, Maia F R N C, Marchesini S, Martin A V, Reich C, Rolles D, Rudek B, Rudenko A, Schlichting I, Schulz J, Seibert M M, Sierra R G, Soltau H, Starodub D, Stellato F, Stern S, Strueder L, Timneanu N, Ullrich J, Wahlgren W Y, Wang X, Weidenspointner G, Wunderer C, Fromme P, Chapman H N, Spence J C H and Neutze R 2012 *Nature Methods* **9** 263

[3] Chapman H N, Fromme P, Barty A, White T A, Kirian R A, Aquila A, Hunter M S, Schulz J, DePonte D P, Weierstall U, Doak R B, Maia F R N C, Martin A V, Schlichting I, Lomb L, Coppola N, Shoeman R L, Epp S W, Hartmann R, Rolles D, Rudenko A, Foucar L, Kimmel N, Weidenspointner G, Holl P, Liang M N, Barthelmess M, Caleman C, Boutet S, Bogan M J, Krzywinski J, Bostedt C, Bajt S, Gumprecht L, Rudek B, Erk B, Schmidt C, Homke A, Reich C, Pietschner D, Struder L, Hauser G, Gorke H, Ullrich J, Herrmann S, Schaller G, Schopper F, Soltau H, Kuhnel K U, Messerschmidt M, Bozek J D, Hau-Riege S P, Frank M, Hampton C Y, Sierra R G, Starodub D, Williams G J, Hajdu J, Timneanu N, Seibert M M, Andreasson J, Rocker A, Jonsson O, Svenda M, Stern S, Nass K, Andritschke R, Schroter C D, Krasniqi F, Bott M, Schmidt K E, Wang X Y, Grotjohann I, Holton J M, Barends T R M, Neutze R, Marchesini S, Fromme R, Schorb S, Rupp D, Adolph M, Gorkhover T, Andersson I, Hirsemann H, Potdevin G, Graafsma H, Nilsson B and Spence J C H 2011 *Nature* **470** 73–U81 ISSN 0028-0836

[4] Vinko S M, Ciricosta O, Cho B I, Engelhorn K, Chung H K, Brown C R D, Burian T, Chalupsky J, Falcone R W, Graves C, Hajkova V, Higginbotham A, Juha L, Krzywinski J, Lee H J, Messerschmidt M, Murphy C D, Ping Y, Scherz A, Schlotter W, Toleikis S, Turner J J, Vysin L, Wang T, Wu B, Zastrau U, Zhu D, Lee R W, Heimann P A, Nagler B and Wark J S 2012 *Nature* **482** 59–62 ISSN 0028-0836

[5] Glover T E, Fritz D M, Cammarata M, Allison T K, Coh S, Feldkamp J M, Lemke H, Zhu D, Feng Y, Coffee R N, Fuchs M, Ghimire S, Chen J, Shwartz S, Reis D A, Harris S E and Hastings J B 2012 *Nature* **488** 603–+ ISSN 0028-0836

[6] David C, Gorelick S, Rutishauser S, Krzywinski J, Vila-Comamala J, Guzenko V A, Bunk O, Farm E, Ritala M, Cammarata M, Fritz D M, Barrett R, Samoylova L, Gruenert J and Sinn H 2011 *Scientific Reports* **1** 57

[7] Nilsson D, Uhlen F, Holmberg A, Hertz H M, Schropp A, Patommel J, Hoppe R, Seiboth F, Meier V, Schroer C G, Galtier E, Nagler B, Lee H J and Vogt U 2012 *Opt. Lett.* **37** 5046

[8] Yumoto H, Mimura H, Koyama T, Matsuyama S, Tono K, Togashi T, Inubushi Y, Sato T, Tanaka T, Kimura T, Yokoyama H, Kim J, Sano Y, Hachisu Y, Yabashi M, Ohashi H, Ohmori H, Ishikawa T and Yamauchi K 2013 *Nature Photonics* **7** 43–47

[9] Schropp A, Hoppe R, Meier V, Patommel J, Seiboth F, Lee H J, Nagler B, Galtier E C, Arnold B, Zastrau U, Hastings J B, Nilsson D, Uhlen F, Vogt U, Hertz H M and Schroer C G 2013 *Scientific Reports* **3** 1633

[10] Yan H and Chu Y S 2013 *J. Synchrotron Rad.* **20** 89–97

[11] Schropp A, Hoppe R, Patommel J, Seiboth F, Uhlén F, Vogt U, Lee H J, Nagler B, Galtier E C, Zastrau U, Arnold B, Heimann P, Hastings J B and Schroer C G 2013 *Proc. SPIE* **8849** 88490R

[12] Lengeler B, Schroer C, Tümmler J, Benner B, Richwin M, Snigirev A, Snigireva I and Drakopoulos M 1999 *J. Synchrotron Rad.* **6** 1153–1167

[13] Lengeler B, Schroer C G, Kuhlmann M, Benner B, Günzler T F, Kurapova O, Somogyi A, Snigirev A and Snigireva I 2004 *Synchrotron Radiation Instrumentation* (*AIP Conference Proceedings* no 705) ed Warwick T, Arthur J, Padmore H A and Stöhr J pp 748–751

[14] Rodenburg J M and Faulkner H M L 2004 *Appl. Phys. Lett.* **85** 4795–4797

[15] Rodenburg J M, Hurst A C, Cullis A G, Dobsen B R, Pfeiffer F, Bunk O, David C, Jefimovs K and Johnson I 2007 *Phys. Rev. Lett.* **98** 034801

[16] Thibault P, Dierolf M, Menzel A, Bunk O, David C and Pfeiffer F 2008 *Science* **321** 379–382

[17] Thibault P, Dierolf M, Bunk O, Menzel A and Pfeiffer F 2009 *Ultramicroscopy* **109** 338–343

[18] Maiden A M and Rodenburg J M 2009 *Ultramicroscopy* **109** 1256–1262

[19] Schropp A, Boye P, Goldschmidt A, Hönig S, Hoppe R, Patommel J, Rakete C, Samberg D, Stephan S, Schöder S, Burghammer M and Schroer C G 2011 *J. Microscopy* **241** 9–12

[20] Giewekemeyer K, Thibault P, Kalbfleisch S, Beerlink A, Kewish C M, Dierolf M, Pfeiffer F and Salditt T 2010 *P. Natl. Acad. Sci. USA* **107** 529–534

[21] Schropp A, Hoppe R, Patommel J, Samberg D, Seiboth F, Stephan S, Wellenreuther G, Falkenberg G and Schroer C G 2012 *Appl. Phys. Lett.* **100** 253112

[22] Hoppe R, Reinhardt J, Hofmann G, Patommel J, Grunwaldt J D, Damsgaard C D, Wellenreuther G, Falkenberg G and Schroer C G 2013 *Appl. Phys. Lett.* **102** 203104

[23] Dierolf M, Menzel A, Thibault P, Schneider P, Kewish C M, Wepf R, Bunk O and Pfeiffer F 2010 *Nature* **467** 436–440

[24] Diaz A, Trtik P, Guizar-Sicairos M, Menzel A, Thibault P and Bunk O 2012 *Phys. Rev. B* **85** 020104(R)
[25] Wilke R N, Priebe M, Bartels M, Giewekemeyer K, Diaz A, Karvinen P and Salditt T 2012 *Opt. Express* **20** 19232–19254
[26] Schropp A, Boye P, Feldkamp J M, Hoppe R, Patommel J, Samberg D, Stephan S, Giewekemeyer K, Wilke R N, Salditt T, Gulden J, Mancuso A P, Vartanyants I A, Weckert E, Schöder S, Burghammer M and Schroer C G 2010 *Appl. Phys. Lett.* **96** 091102
[27] Kewish C M, Guizar-Sicairos M, Liu C, Qian J, Shi B, Benson C, Khounsary A M, Vila-Comamala J, Bunk O, Fienup J R, Macrander A T and Assoufid L 2010 *Opt. Express* **18** 23420–23427
[28] Kewish C M, Thibault P, Dierolf M, Bunk O, Menzel A, Vila-Comamala J, Jefimovs K and Pfeiffer F 2010 *Ultramicroscopy* **110** 325–329
[29] Vila-Comamala J, Diaz A, Guizar-Sicairos M, Mantion A, Kewish C M, Menzel A, Bunk O and David C 2011 *Opt. Express* **19** 21333–21344
[30] Hönig S, Hoppe R, Patommel J, Schropp A, Stephan S, Schöder S, Burghammer M and Schroer C G 2011 *Opt. Express* **19** 16325–16329
[31] Schroer C G, Boye P, Feldkamp J M, Patommel J, Samberg D, Schropp A, Schwab A, Stephan S, Falkenberg G, Wellenreuther G and Reimers N 2010 *Nucl. Instrum. Meth. A* **616** 93–97
[32] Schropp A, Patommel J, Seiboth F, Arnold B, Galtier E C, Lee H J, Nagler B, Hastings J B and Schroer C G 2012 *Proc. SPIE* vol 8504 p 85040F